RESEARCH ARTICLE

A cable-driven soft robotic end-effector actuator for probe-based confocal laser endomicroscopy: Development and preclinical validation

Charles DeLorey[1] | **Joseph D. Davids**[1,2] | **Joao Cartucho**[1] | **Chi Xu**[1] |
Alfie Roddan[1] | **Amr Nimer**[3] | **Hutan Ashrafian**[1] | **Ara Darzi**[1] |
Alex James Thompson[1] | **Saina Akhond**[1] | **Mark Runciman**[1] |
George Mylonas[1] | **Stamatia Giannarou**[1] | **James Avery**[1]

[1]Institute of Global Health Innovation and the Hamlyn Centre for Robotic Surgery, Imperial College London, London, UK

[2]National Hospital for Neurology and Neurosurgery, London, UK

[3]UKRI Centre for AI in Healthcare, Imperial College London, London, UK

Correspondence
Dr James Avery and Stamatia Giannarou, Institute of Global Health Innovation and the Hamlyn Centre for Robotic Surgery and Artificial Intelligence, Imperial College London, South Kensington, Exhibition Road, London SW7 2AZ, UK.
Email: james.avery@imperial.ac.uk, stamatia.giannarou@imperial.ac.uk

Abstract

Soft robotics is becoming a popular choice for end-effectors. An end-effector was designed that has various advantages including ease of manufacturing, simplicity and control. This device may have the advantage of enabling probe-based devices to intraoperatively measure cancer histology, because it can flexibly and gently position a probe perpendicularly over an area of delicate tissue. This is demonstrated in a neurosurgical setting where accurate cancer resection has been limited by lack of accurate visualisation and impaired tumour margin delineation with the need for in-situ histology. Conventional surgical robotic end-effectors are unsuitable to accommodate a probe-based confocal laser endomicroscopy (p-CLE) probe because of their rigid and non-deformable properties, which can damage the thin probe. We have therefore designed a new soft robotic platform, which is advantageous by conforming to the probe's shape to avoid damage and to facilitate precision scanning.

KEYWORDS

actuation, brain tissue characterisation, end-effector, p-CLE, soft robot, brain tumours

---
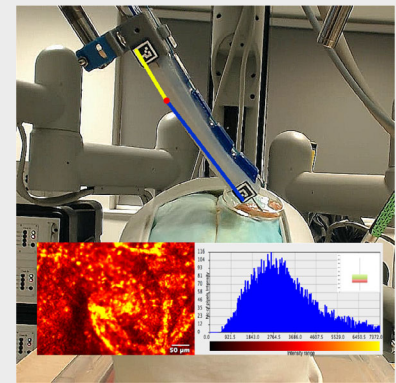
Charles DeLorey and Joseph D. Davids are joint first authors.

Mark Runciman, George Mylonas, Stamatia Gianarrou and James Avery are joint supervising authors.

1 | INTRODUCTION

Breakthrough robotic surgical platforms such as the Da Vinci from Intuitive Surgical were designed initially to

focus on general surgical, ear nose and throat and uro-logical procedures where they have seen widespread adoption [1–15]. Neurosurgery is yet to fully embrace robotic surgery for precision tumour resection with a growing interest in paediatrics and epilepsy surgery, but the earliest attempts leveraged the PUMA 560 for brain tumour biopsies [16–22]. To overcome challenges in achieving gross total resection and excision margin delineation affecting tumour recurrence and poor prognosis, other real-time in-situ optical and endoscopic methods have been proposed such as two-photon microscopy and Raman spectroscopy [19, 20, 23, 24]. Probe-based confocal laser endomicroscopy (p-CLE) for in-situ histology is such a method that can be used to differentiate cancer from normal tissue and guide precision surgery [25–33].

The challenge is that the thin p-CLE probes have to be positioned perpendicularly to the tissue being sampled to obtain high quality images. It is difficult to manoeuvre thin p-CLE probes and maintain perpendicular positioning while minimising tissue trauma from contact forces on the surface of the tissue, thus limiting precision image measurements. Hence, soft robotic end-effectors are rising in popularity as a solution in this area [34, 35]. The end-effector of the robot usually refers to the distal end of the robotic arm required to perform an interactive function with the target object of interest, including for instance, grippers, force-torque sensors, material removal tools and collision detection systems [36].

The resection of cancers, such as those located in the brain, is usually associated with narrow surgical corridors that affect lesion visibility and instrument manoeuvrability.

Robotic end-effector systems have been designed for various robotic platforms such as the Da Vinci to allow tissue manipulation. Other end-effector applications such as camera systems have included separate fixed modules on the Da Vinci, but with the invention of handheld microscopy and spectroscopy probes for in-situ surgical imaging, new end-effector systems have become necessary. Da Vinci end-effectors were not designed for probe-based confocal laser endomicroscopy so currently no designs exist to hold, manoeuvre and accurately position the probe perpendicular to the tissue of interest.

Handheld manipulation of probes such as a 0.65 to 1.8 mm confocal endomicroscopy probe, a tool used for real-time histological imaging, presents a cumbersome challenge to the surgeon who has multiple intraoperative tasks occurring concurrently. Not only does the surgeon have to take their eyes off the surgical field to monitor the location of the tip of the endomicroscopic tool on a separate viewport, but they must simultaneously direct the probe to the area of interest. Some of these rigid probe designs cannot bend within the narrow confines of the resection corridor to scan around corners within a resection cavity and have a limited bending radius. Other limitations include blind-ended entry where the surgeon has little visibility of the probe-tip in a resection cavity for a measurement, which increases the risk of injury to the surrounding structures and also increases the margin for measurement error.

The lack of flexibility of the thin probe can cause the probe to slip or slide from its target, requiring subtle micrometre to millimetre adjustments that are difficult to achieve and thus increase the risk of measurement error. These minute adjustments can affect the image quality, leading to misclassification in computer vision for pathologies such as tumours. This challenging problem is compounded by the fact that probes should be able to bend into a curved shape to image a region of interest. This is also particularly difficult during tissue scanning using rigid end-effector systems.

Robotic actuation of a flexible end-effector eliminates these challenges by increasing the degrees of freedom afforded to the surgeon during a measurement. However, very minimal developments have been made in the field of surgical soft robotics and its application to neuro-oncology. The motivation for soft robotics instead of rigid robotic systems relates to the low stiffness of the soft material, similar to human tissue stiffness, which can potentially reduce excessive pressure or force on the tissue [35, 37, 38]. Soft robots also potentially afford more degrees of freedom. A variety of methods for sensing and actuation exist, and computer vision-based sensing with cable driven actuation offers a low-cost and repeatable approach. Low-cost surgical robots have the potential to democratise robotics and make surgical education affordable [15].

In this work we have designed a soft robotic end-effector that has potential advantages such as ease of manufacture, simplicity and electronic control. This device offers advantages in controlling new probe-based devices, because it can gently and flexibly place them in contact with delicate tissues. As an initial demonstration of this capability, we explore whether the device could be used in neurosurgery to support confocal endomicroscopic probe manipulation and tissue scanning, referred to as an optical biopsy.

2 | MATERIALS AND METHODS

2.1 | Soft robot design

The functional design of this soft robot actuator was intended for applications in grasping tasks and prosthetics. The actuator design includes a hollow chamber running along the length of the actuator.

2.2 | Manufacturing process

The robotic actuator was designed to be similar to a finger with flexion and extension movement. The actuator
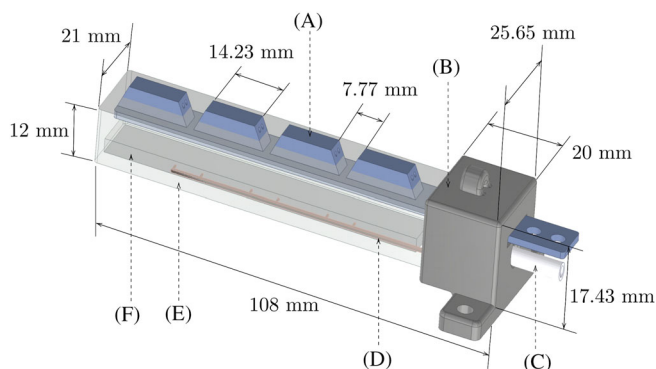
FIGURE 1 Colour rendering of the assembled soft robot actuator (units: mm). Features labelled are the (A) 3D printed flexible backbone, (B) actuator mounting, (C) saline inlet, (D) electrode wires, (E) silicone actuator body and the (F) saline chamber. All measurements are in millimetres

body was manufactured using soft, flexible silicone (EcoFlex 00-20, Smooth-On Inc., Macungie, PA) with an internal backbone piece of 3D-printed flexible plastic (NinjaFlex, Ninjatek, Manheim, PA), using a process called shape-deposition manufacturing (SDM). This technique allows the integration of non-silicone parts or subsystems into individual fabrication steps, the flexible backbone piece being one such part. This backbone piece provides structure to the actuator and enables the cable-driven actuation method. A thin cable is affixed to the actuator tip, threaded through holes running along the length of the actuator through the raised trapezoidal shapes of the backbone (Figure 1A). This silicone and flexible plastic assembly is held in place with a hard plastic mount, through which the cable is threaded. When the cable is pulled, the length of the cable decreases, pulling the tip of the actuator towards the base in a curling motion, producing a finger-like actuation trajectory.

2.3 | The manufacturing was performed in five stages

1. Electrodes (0.1 mm diameter enamelled copper wires, Figure 2i) were placed in the mould (Figure 2A) and silicone was added to cast them in place for one side of the saline chamber.
2. A layer of cast silicone was glued to the open side of the previous part, sealing it (Figure 2B).
3. The now sealed chamber was placed into and pushed down in the encasing mould (Figure 2C). A flexible backbone was set in place atop the chamber and more silicone was added to cast the backbone and the chamber together as one actuator.

4. The fully cast actuator was removed from the mould (Figure 2D). A hole was cut in the base of the actuator into the hollow chamber and a flexible plastic tube was inserted and glued into place, to serve as the saline inlet (Figure 2E,ii).
5. A 3D-printed hard plastic mount (Figure 2iii) is fit around the base of the actuator (Figure 2F). A thin cable (Figure 2iv) is threaded through the holes on the flexible backbone for actuation.

The 3D-printed moulds were designed and fabricated to cast the various parts needed, including a chamber in which to place electrodes and the saline solution. This chamber was placed along the length of the actuator on the posterior side of the soft robot actuator, where the saline chamber was located. The flexible backbone had two parallel series of holes, which run through the length of each joint for guiding the cable. When a cable was threaded through and pulled, the backbone would bend away from its flat side. The soft actuator was driven using a stepper motor, which pulled the length of cable affixed to the tip of the actuator. The mechanical properties of the soft robot actuator silicone include a shore hardness of 0 to 20, a tensile strength of 160 psi and 100% modulus of 8 psi [39].

2.3.1 | Sensing

While not utilised in this paper, the soft robot actuator was designed with shape sensing capabilities for sensing deformation when actuated [40]. This sensing subsystem consists of the silicone chamber (which would be filled with saline) with six electrode wires embedded into the silicone, and a tube inlet. These six wires protrude into the chamber and enable a sensing technique called electrical impedance tomography (EIT) [40, 41]. To simplify the experimental procedure and results of this work, the sensing portion of the robot is omitted and treated separately, and the saline chamber is instead used to house the flexible p-CLE probe. The Lumen of the soft robot was 1.5 mm diameter, which allowed the p-CLE probe to be held.

2.3.2 | 3D printing of skull and craniotomy

The 3D printed skull was created using DICOM data from a human head CT that was uploaded into an.stl (STereoLithography) file in 3D Slicer software (Version 4.5, Slicer Community). This was then loaded into Blender software (Version 2.78, Blender Foundation), where unwanted and unnecessary data (such as the structures beneath the skull base) were digitally removed.
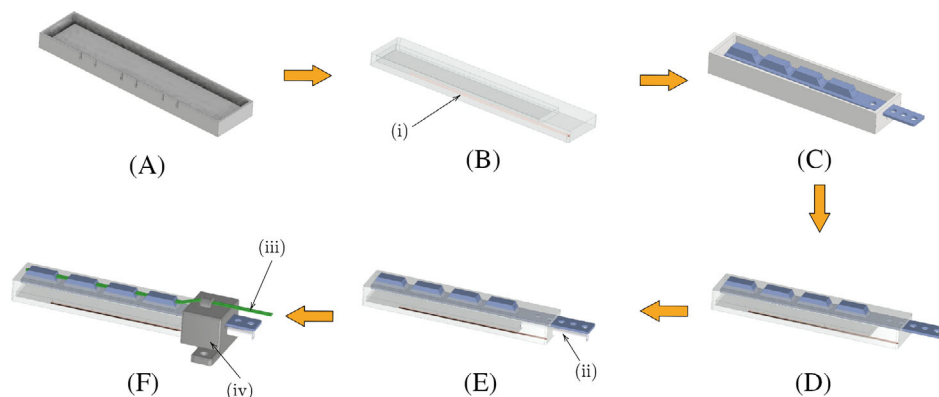
FIGURE 2 Flowchart diagram of manufacturing process of soft robotic actuator. The 3D-printed mould for making the unsealed chamber with embedded electrodes (A), and the cast chamber (B), the mould with a flexible backbone piece in place (C), the resulting fused together silicone and flexible plastic actuator (D), that same actuator with a plastic tube inlet (E, ii), a cable for actuation (F, iii) and workspace mount (iv)

A section of skull "bone window" was removed from the model and subtracted from a cuboid structure to create a hollow volume to be used as a cast. The cuboid was then halved along the direction of the void, thereby creating a cast. The ventricle system was also rendered using the techniques described above. The data (in .stl form) was then "cleaned" and any gaps in the data were eliminated, that is, any bone fragments "floating" in the file, which would make the. stl file unprintable, were removed. The resulting files were printed on an Eden 260 V 3D printer (Stratasys Ltd., USA) with the photopolymer Med 610 material using PolyJet technology.

Creating a "bone window" allows for multiple usages of the same model base. If the area of the skull to be drilled/craniotomy (in the case illustrated above, the frontal region) is to be made of expendable material, the material could be replaced after each use, leaving the actual base model intact and available for reuse. To find a material that has a bone-like structure and feel, various forms and types of gypsum plaster were manufactured and experimented with in a laboratory. The plaster mixtures were added to water and set in plates to harden, after which their hardness was tested using a drill. The likeness of the material to bone was tested by six independent senior neurosurgeons.

To manufacture the expendable material, we implemented the following regime:

1. 50 g of the articulation plaster was added to a bowl.
2. 2 g of bentonite was crushed into a fine powder, and the powder then added to the bowl with the plaster.
3. Twenty five millilitres of water was added and mixed vigorously.
4. The mixture was then placed on a vibrating machine to remove air bubbles for 10 to 20 seconds.
5. While still in liquid form, the mixture was poured into the cast and allowed to set for 75 to 90 minutes, depending on room temperature.
6. To simulate the internal table of the bone, a thin layer of epoxy resin was added to the inside of the plaster cast using a fine brush, and allowed to dry.
7. A thin rubber sheet was glued on the top of the cast to mimic the periosteum. Any unwanted plaster on the edges was cut with a plaster scissor.
8. The cast would then fit snugly on the bone window of the 3D printed skull.

Figures 3, 4, 6 and 7 illustrate the 3D-printed skull model with a bi-frontal craniotomy window presenting imaginary surgemes highlighted in Figure 7. Surgemes are equal areas of simulated imaginary divisions at the bifrontal craniotomy window for which measurements are acquired for analysis to enable objective quantification of trajectories in an *X-Y* plane.

2.3.3 | Da Vinci setup

The Da Vinci Surgical System (Intuitive Surgical, Sunnyvale, CA) is a teleoperated surgical robot for minimally invasive surgery (MIS) [42, 43]. The system consists of two robotic manipulators that rest in the operating range (Figure 3A), a console with joystick-like controls for the robot arms as well as stereo vision for the operator, and an intermediate control system, which facilitates robot arm control and stabilisation, and other such tasks. While the Da Vinci robot was powered and engaged for the experiments in this paper, the tele-operative capabilities were not used, but instead the self-stabilising feature of the robot arms served as an adjustable base for the soft robot and
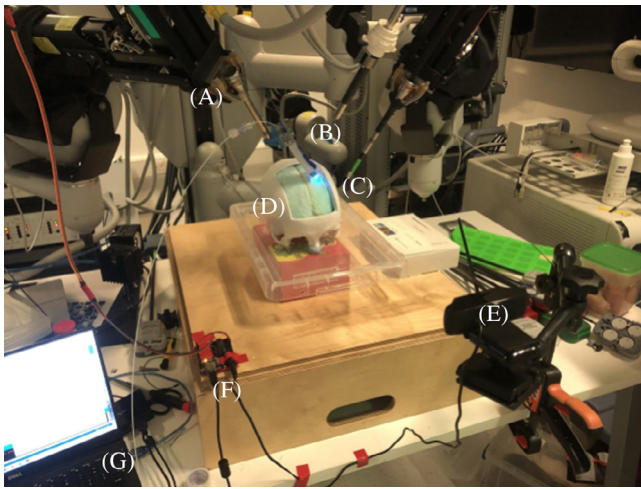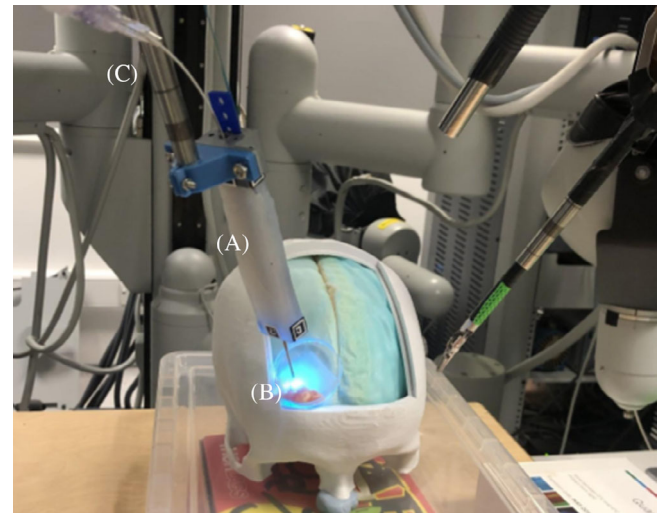
FIGURE 3 Wide view of soft robot experimental setup on a da Vinci surgical robot (A), with the soft robot (B) affixed to the Da Vinci robot, containing the p-CLE probe (C), a brain model (D), webcam (E) for recording experiments, the microcontroller (F) that controls the soft robot, and a laptop (G) where the recording and soft robot actuation are controlled. p-CLE, probe-based confocal laser endomicroscopy

FIGURE 4 Closeup view of soft robot actuator system (A) and p-CLE probe (B) affixed to the end of the da Vinci robot arm (C). p-CLE, probe-based confocal laser endomicroscopy

probe system. The soft robot was affixed to the distal end of the left-hand Da Vinci robot arm, and the mock skull model was placed below it (Figure 4). The webcam and soft robot were controlled on the same laptop using a Python script and an Arduino program, respectively.

2.4 | Operation/control and robotic vision

The cable-driven actuation of the robot was controlled using keyboard input to a microcontroller-powered system (Arduino Uno, Arduino Inc., Somerville, MA), which drove a stepper motor pulling on the cable, as shown in Figure 5A. To ascertain the bending angle achieved by the soft robot, a series of computer vision point tracking markers were used. Pairs of these markers (ArUco optical markers, The OpenCV Library. *Dr. Dobb's Journal of Software Tools*) were placed on the four sides of the actuator, one at the base and one at the actuator tip, to ensure full coverage in non-perpendicular views of the robot for computer vision purposes during these experiments. Point estimations in space were found and from these points bend angle values were computed. The functional range of angles achievable by the soft robot is between 1.6° (robot lying flat) and 143° (robot bent). This bending angle achieved by the robot is defined as the angle between the line that intersects the two bottom corners of the base marker and the line that intersects the two bottom corners of the fingertip marker, in the plane

of the markers affixed to the viewable side of the robot (illustrated in Figure 5B).

The values presented in Table 1 were computed by finding the x, y coordinates of the marker at the tip of the robot for each recorded frame in the footage of the experiment. The footage was captured at 40 frames per second (fps) and the ArUco markers are 10 mm squares, from which the trajectory of the robot tip was computed. The positions of the markers enabled calculation of the velocity, which in turn is used to compute acceleration and then used to find the jerk, the equations of which are described below. While not explored in depth in this work, the inherent complication of discrete modelling of soft robots is because of their flexible construction. In our design, the hinged backbone with discrete segments means the soft robot is constrained to move in a plane.

The velocity, acceleration and jerk measurements were computed using the series of equations as described below, with v = velocity, $\underline{v}$ = mean velocity, a = acceleration, $\underline{a}$ = mean acceleration, j = jerk and $\underline{j}$ = mean jerk.

Equation 1 shows the calculation of the velocity at the point with the coordinate (x_i, y_i), i being the frame index, which in this case is the coordinate of the optical marker placed on the distal end of the end-effector. Change in frame number with respect to change in time is expressed as dt.

$$v_i = \sqrt{\left(\frac{x(i+1) - x(i)}{dt}\right)^2 + \left(\frac{y(i+1) - y(i)}{dt}\right)^2}. \quad (1)$$

Equation (2) computes the mean velocity over all frames 1 to n, n being the total number of frames in the experimental footage.
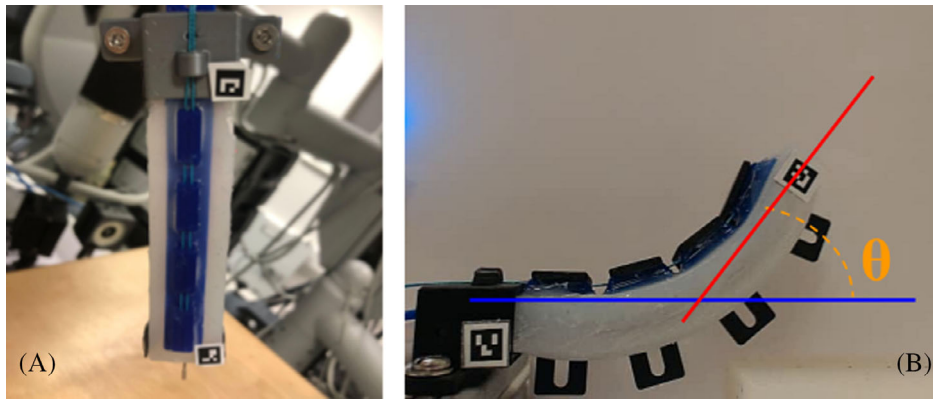
FIGURE 5 (A) Soft robotic actuator with ArUco markers for angle estimation using computer vision. (B) Illustration of derivation of target angle θ, showing how much the robot bends and the associated formulae used to calculate the metrics of bending, velocities, acceleration and jerk

$$\underline{v} = \frac{1}{n}\sum_{i=1}^{n}(v_i). \qquad (2)$$

Equations (3) to (6) accomplish similar calculations, deriving the acceleration at each timestep i in the footage (Equation 3), finding the mean acceleration (Equation 4), the jerk at each timestep in the footage (Equation 5) and the mean jerk (Equation 6).

$$a_i = \left(\frac{v(i+1) - v(i)}{dt}\right), \qquad (3)$$

$$\underline{a} = \frac{1}{n}\sum_{i=1}^{n}(a_i), \qquad (4)$$

$$j_i = \left(\frac{a(i+1) - a(i)}{dt}\right), \qquad (5)$$

$$\underline{j} = \frac{1}{n}\sum_{i=1}^{n}(j_i). \qquad (6)$$

2.4.1 | Ethical approval

Approval was granted by the University and Regional Ethics Committees in London England for ex vivo tissue usage (IRAS ID 215417).

2.4.2 | Probe-based confocal laser endomicroscopy

The probe-based confocal endomicroscopy tool is an optical technique that allows in-situ histopathological optical biopsies to be achieved in real time. Image acquisition using the Probe-based Confocal Laser

Endomicroscopy was performed with the Cellvizio 488 nm wavelength pre-clinical p-CLE, 1.5 mm diameter s-1500 probe (Mauna Kea Technologies, France), calibrated and run using their Image Cell software (version 3.8.4) running on Apple Inc San Francisco MacBook pro OS X 10.9.5 Mavericks, due to software upgrade challenges and restrictions from the manufacturer and a requirement to power the p-CLE CellVizio laser system.
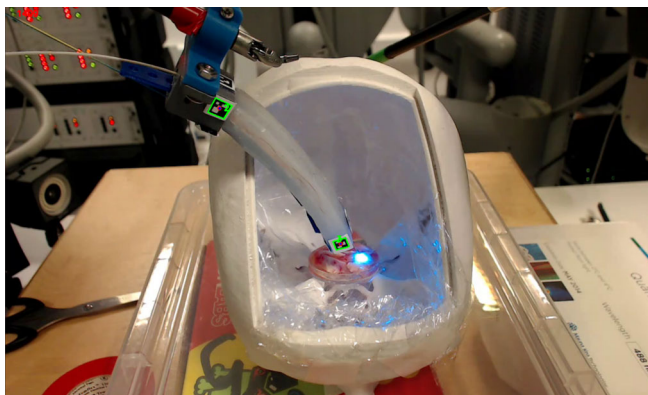
Figures 2 and 3 summarise our ex vivo set-up. Ex vivo experiments for image acquisition were performed on porcine brain tissue, which was obtained from the local butcher. Thin scalpel-cut 1 mm cortical slices of 2 cm × 2 cm squares were placed in a 4 cm petri dish and stained with 0.1% acriflavine for 1 minute. The tissue surface was washed with 2 mL phosphate buffered saline (Gibco PBS, Thermo Fisher Scientific, Waltham, MA) for a further 30 seconds prior to imaging to remove excess acriflavine. Additional custom-built image capturing and pre-processing scripts were written in Python (version 3.6) and MATLAB (MATLAB version 2019b, The MathWorks Inc., Natick, MA) to facilitate batch image processing. Images were acquired from the p-CLE probe at a frame rate of 11.8 fps to reduce the size of the files and to expedite post-acquisition image processing. Image clarity was processed using the no perceptual blur metrics filters available through MATLAB. The clarity and intensity measurements were computed as means, standard deviations, medians and interquartile ranges between hexemes. The Kruskal-Wallis nonparametric statistical test was used to assess differences between hexeme distributions with significance set at $P < .05$.

2.4.3 | Segmental (hexeme) range assessment

The craniectomy window was divided into six imaginary planes for porcine tissue positioning and simulation and to compute bend angle measurements for each hexeme. Dexterity of the robotic arm was measured with respect

TABLE 1 Summary table of dexterity measurements organised by hexeme method of data acquisition illustrating safety parameters such as forces exerted by the robot, velocity, acceleration and jerk measurements and scanning profiles such as bend angle

Region sampled		Hexeme 1	Hexeme 2	Hexeme 3	Hexeme 4	Hexeme 5	Hexeme 6
Distance of tissue from the midline (mm) (x, y)		21 across in x-direction, 18 down in the y-direction	21 across in the x-direction, 5 up in the y-direction	30 across in x-direction, 9 down in the y-direction	21 across in the x-direction, 11 up in the y-direction	21 across in the x-direction, 4 up in the y-direction	23 across in the x-direction, 5 up in the y-direction
Mean velocity	(pixel/s)	18.9	0.0	17.2	14.5	0.0	0.0
	pixels SD	63.1	0.0	38.1	28.0	0.0	0.0
	(mm/s)	10.8 [0.0108]	0.0	10.4 [0.0104]	6.9 [0.00692]	0.0	0.0
	mm SD	36.1	0.0	23.1	13.3	0.0	0.0
Mean acceleration	(pixel/s^2)	-1.48×10^{-14}	0.0	-18.4	-6.89×10^{-15}	0.0	0.0
	pixel SD	3375.039		1893.825	1083.952		
	(mm/s^2)	-8.49×10^{-15} [-8.49×10^{-18}]	0.0	-11.2 [-0.0112]	-3.28×10^{-15} [-3.28×10^{-18}]	0.0	0.0
	mm SD	1932.542		1148.300	515.583		
Mean jerk	(pixel/s^3)	-1.58×10^{-12}	0.0	737	4.41×10^{-13}	0.0	0.0
	pixel SD	228 645.453		124 378.255	65 714.270		
	(mm/s^3)	-9.06×10^{-13} [-9.06×10^{-16}]	0.0	447 [0.447]	2.10×10^{-13} [2.10×10^{-16}]	0.0	0.0
	mm SD	130 922.006		75 415.395	31 257.091		
Mean force (g mm/s^2) [N]		-2.76×10^{-13} [-2.76×10^{-19}]	0.0	-363 [-0.000363]	-1.07×10^{-13} [-1.07×10^{-19}]	0.0	0.0
Bend angle (°)		19.7	6.08	2.91	1.58	0.195	6.72

FIGURE 6 Interior tissue sample experiment using soft robot actuator with labelled AruCo markers attached to the DaVinci robotic arm

to the midline and orientation of the end effector and was achieved using computer vision. The sampled sites in each hexeme were measured in horizontal and vertical distance from where the horizontal diameter of the dish intersects the circumference of the dish as shown in Figure 8.

3 | RESULTS

The dexterity of the soft robot is measured using a hexeme division approach at the bi-frontal craniotomy window and is presented in Table 1. The calculated perimeter of the achieved polygonal area in Figure 10 is 0.233 m, and the surface area is 0.00321 m^2. The mean force exerted during actuation by the probe was calculated from the equation $F = m * a$, using the computed mass of the soft robot and the mean acceleration found. The mass of the robot was found to be 0.0325 kg, using the equation $m = d * V$ where density $d = 1070$ kg/m^3 and $V = 3.04 \times 10^{-5}$ m^3. The velocity, jerk, acceleration and forces across each hexeme are reported in Table 1. Maximum velocity was seen across hexeme 1 at 0.0108 m/s, generating a bend angle of 19.7° and with maximum acceleration seen across hexeme 3 at -0.0112 m/s^2 at an estimated force of -0.000363 Newtons.

3.1 | Results from optical biopsy

Table 2 and Figure 11 summarise results from the optical biopsy of porcine brain tissue during the robotic assisted p-CLE acquisition, which illustrates on the *Y*-axis the number of pixels with a given signal intensity, where the *X*-axis is the range of signal intensities measured. Hexeme 1 had a median intensity of 1813 pixels (LQ = 1398,

UQ = 2398, IQR = 1000). Hexeme 2 demonstrated the highest median intensity value of 3091 pixels (LQ = 2219, UQ = 4206, IQR = 1987). Hexeme 3 had a comparatively lower median intensity value of 2016 pixels (LQ = 1431, UQ = 2734, IQR = 1303) to hexeme 4, which showed the second highest median intensity value at 2397 pixels (LQ = 1789, UQ = 3023, IQR = 1234). Hexeme 5 had the lowest median intensity value of 367 (LQ = 206, UQ = 771, IQR = 565) compared to hexeme 6 with a value of 572 pixels (LQ = 383, UQ = 780, IQR = 397).

4 | DISCUSSION

Clinical application of soft robotics as end-effectors is increasing. In our work we designed an end-effector system to demonstrate the various advantages ranging from ease of manufacturing, simplicity and electronic control tackling a case for image acquisition within a tumour resection cavity. Our device may have the advantage of guiding and enabling fragile probe-based devices to intraoperatively measure cancer histology by offering flexibility with gentle perpendicular position of the probe over an area of delicate tissue. We demonstrated this use-case in a neurosurgical setting where accurate cancer resection has been limited by lack of accurate cellular visualisation. We tested this by using a p-CLE probe to acquire images and test their clarity.

Soft robots such as our platform are composed of flexible or compliant materials, enabling behaviours and actuation patterns different from traditional rigid robots [37, 44]. Research and clinical applications of these technologies are still young, as soft robot systems present new challenges in motion control and system modelling. Owing to their deformable nature, soft robot systems are well-suited to surgical robot applications as they do not exert the same direct and concentrated forces as rigid devices would, instead deflecting to similarly flexible tissue around them. Our platform may therefore be more suitable for the brain and resecting tumours. Tumours of the brain present a significant intraoperative diagnostic challenge affecting margin delineation, which curtails the principles of maximising the extent of intraoperative resection known to improve survival. Probe-based confocal laser endomicroscopy is one such emerging technique that has garnered histopathological capability to differentiate tumour from normal [25–28, 31, 32].

However, handheld manipulation of a 0.65 to 1.8 mm confocal laser endomicroscopy probe presents a challenge to the surgeon who is handling multiple intraoperative tasks concurrently. To trigger a measurement, the surgeon has to take their eyes off the surgical field to monitor the location of the tip of the endomicroscopic tool on a separate

FIGURE 7 (A-F) p-CLE measurements sampling each region h1-h6. (G) Hexeme regions on craniectomy window (frontal view of window). p-CLE, probe-based confocal laser endomicroscopy
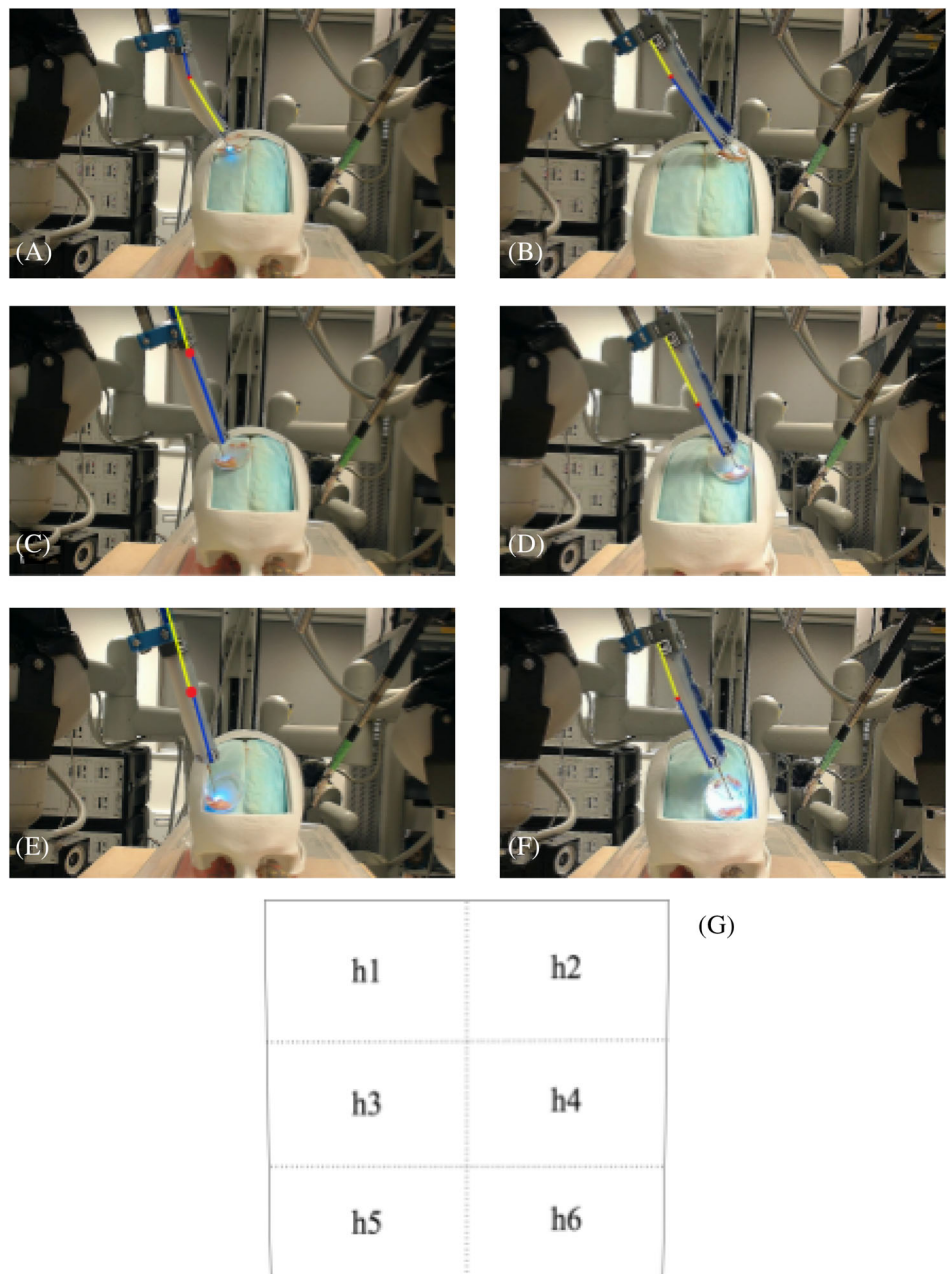

viewport and simultaneously direct the probe to the area of interest, which cannot bend to scan around corners.

The limited flexibility of the p-CLE probe allows for the proposed soft robot to encapsulate it and actuate, bending around obstacles (Figure 5). The actuator is shown to be able to achieve greater than 100° of bending, enabling U-turn-like trajectories to reach regions of interest for optical biopsy. This is much safer for the patient and can be controlled by the surgeon. In our work the desired angle was achieved before experimental recording, which was done solely to acquire angle data of the soft robot. We assessed the bend angle of the robot when attempting to biopsy regions deeper within the cranial cavity (Figure 6 shows the first in these experiments),

through the bi-frontal craniotomy window, and achieved angles for these trials ranging from 41.7° to 112° for this particular intracranial 3D printed skull model (Figure 9). While this soft robot actuated p-CLE probe is more dexterous and capable of reaching larger surface areas than rigid or non-actuated endoscopic systems, the nature of its planar movement is the primary limitation to its capabilities.

In our work, no velocity, acceleration or jerk values are reported for hexemes h2, h5 and h6, because no actuation was performed in these hexeme experiments. Jerk was more pronounced in hexeme 3, which was the highest measurement of this metric, which correlates with the measured forces as illustrated in Table 1. The highest intensity distribution using the hexeme approach was seen for
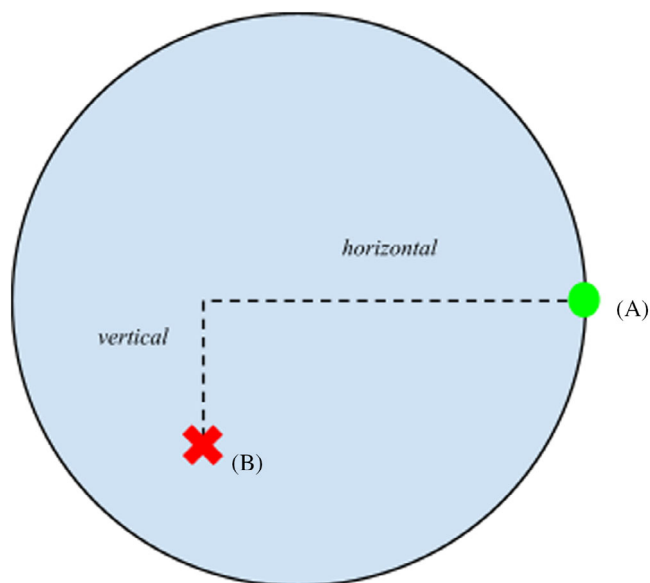
FIGURE 8 Measurement method of sampled region within hexeme division, showing base point (A) measured across the Petri dish and either up or down from that centreline to sample site (B)

h2. The hexeme method allowed us to label and effectively characterise areas of interest within the craniotomy window for analysis. Median values were used because of the skewed distribution of intensities making the Kruskal-Wallis test a superior measure for characterising hexeme differences. A $P = .000$ for differentiating between image intensity across hexemes was observed suggesting the hexeme approach offers an objective measure that can be explored further in simulated craniotomies for robotic p-CLE measurements.

The use of soft materials provides many benefits in robot design and behaviour. Robots made of soft materials in contact with delicate tissues (brain tissue in particular) are able to distribute contact forces over a wider area, exerting less targeted force to tissues [35, 37, 38]. In contrast, when robots made of rigid components such as metals exert force on comparatively softer tissues, it is the tissues that will deform first, resulting in potential damage. Cable-driven actuation such us our method is relatively straightforward and with adequate hardware and sensors can achieve high precision movement [45]. It also enables the means of actuation used to be placed away from the robot, reducing the profile and surface area of devices in the operating field that may require extensive cleaning or sterilisation as well as unnecessary bulk. Indeed, a cable-driven or even fluidically powered actuation system would enable a design free of ferrous materials, allowing the device to be used in magnetic resonance imaging scenarios [36, 45, 46]. However, as shown through the large and variable mean jerk values reported in Table 1, the stepwise cable actuation method

requires re-evaluation to achieve better smoothing motion of the soft robot. Due to the continuous nature of soft robot materials and actuation methods, developing robust control schemes and sensing methods still limit the performance of these soft robot systems.

In contrast to traditional components of rigid robots, soft robots such as this exploit their flexible and compliant mechanical properties. This allows them to achieve novel actuation trajectories and eliminate harmful force applications to surrounding materials with our forces being negligibly small. This is applicable in minimally invasive surgery for navigating a region of interest in surgical scenarios [36, 44]. However, while this nonlinear behaviour enables such flexibility and distribution of forces in contact with delicate tissues, soft robots are notoriously more complex to model computationally and to control with the same level of precision and repeatability as rigid robots [44]. As developments in soft robot technologies advance, including modular or variable stiffening, biocompatible materials, and motion control methods, their applications to medicine and surgery become more and more plentiful. Recent work in soft surgical robots has focused on developing MR (magnetic resonance)-compatible robots as well as exploiting a modular robot design approach [46, 47]. Actuation methods for soft robots include cable actuation, shape memory alloys, fluid elastomers, and dielectric elastomers, each with their own benefits and drawbacks [47]. Likewise, sensing methods for soft robots are important for adequate sensory feedback of the robot, but must not interfere with the robot's performance [47].

Soft or otherwise highly articulated robots (such as continuum robots) are being explored in neurosurgical tasks. Soft robotic end-effector systems are practical for neurosurgical applications as they offer significant advantages over rigid body systems because they are much safer and reduce the amount of pressure placed on the brain tissue during retraction. The sensitivity for soft tissues and MR-compatibility make soft-robotic methods attractive for such a field. Continuum soft robots, which can accomplish trajectories akin to that of an elephant's trunk or octopus arm with their infinite degrees of freedom, allow them to navigate complex regions. Kim and colleagues present a neurosurgical continuum robot actuated using shape memory alloy actuators, capable of segmental control and navigation within a region of interest [46].

4.1 | Limitation and future work

As evidenced by the limited mobility of this prototype, the soft robot was designed for gripping tasks, not

TABLE 2 Summarises data for each hexeme computed for the intensity distributions of the image lookup tables acquired from the p-CLE optical biopsy, displayed as mean $\pm$ SD

Statistical metric	Hexeme 1	Hexeme 2	Hexeme 3	Hexeme 4	Hexeme 5	Hexeme 6
Min	−220	361	326	109	−208	−543
Q1	1398	2219	1431	1789	206	383
Mean	2032	3404	2170	2415	735	592
SD	982.81	1668.58	964.35	975.68	976.89	313.58
Median	1813	3091	2016	2397	367	572
Q3	2398	4206	2734	3023	771	780
Max	8191	8191	8191	7307	8191	2586
FibreCount	11 519	11 519	11 519	11 519	11 519	11 519
IQR	1000	1987	1303	1234	565	397

Notes: Q1 is the lower quartile, Q3 is the higher quartile and IQR is the interquartile range used for Kruskal Wallis analysis of differences. The $P = .000$ demonstrate statistically significant difference between hexemes supporting its effectiveness. The minimum is min and maximum values are max. The look-up tables compute the range of intensities across the region of interest selected within a p-CLE image. In this case the entire frame's look up table values was calculated as a histogram as demonstrated in Figure 10. The fibre count illustrates the number of fibres that were optically triggered to transmit laser light during the p-CLE image acquisition.

Abbreviation: p-CLE, probe-based confocal laser endomicroscopy.

FIGURE 9 Histogram of maximum achieved bending angles by soft robot probe during in-cavity optical biopsy experiments. A summary of experimental robot bending in a series of optical biopsy measurements of samples within the skull to simulate accessing deep skull base lesions from a frontal approach
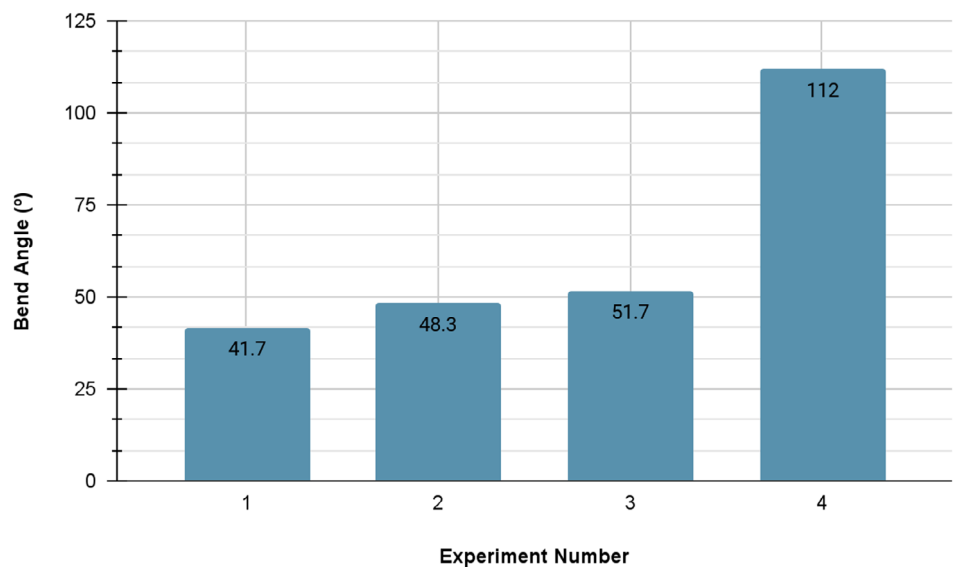

medical instrumentation. This is a proof-of-concept so the dimensions of the robot are larger than necessary, and future redesign and miniaturisation are also feasible to reduce the size of the device for clinical practice.

Further design iterations of this robot would explore an octopus arm-like actuation pattern, referred to as a continuum robot, enabling actuation in any direction regardless of current robot orientation in a space. Such a design would also enable improvement of the reachable workspace of the robot, refining the range of degrees it can reach with the tip. Additionally, the form factor of the soft robot would be reduced significantly to better function in limited space surgical environments, while

still being able to deliver instruments such as optical biopsy probes to the region of interest.

The bending sensor was not used in these experiments, as more design refinement and characterisation are needed for that subsystem and will be integrated in future work. Furthermore, a redesign and recharacterisation of a sensing subsystem are needed not only to properly accommodate and sense a continuum motion scheme of the soft robot, but also for the incorporation of additional hardware such as a p-CLE or Raman endoscopic probe. Future extensions of this soft robot actuator will explore machine learning methods for vision characterisation in soft-robotic probe-based confocal laser endomicroscopic

FIGURE 10 Hexeme sampling sites plotted on coordinate plane in mm showing achieved area in brain window
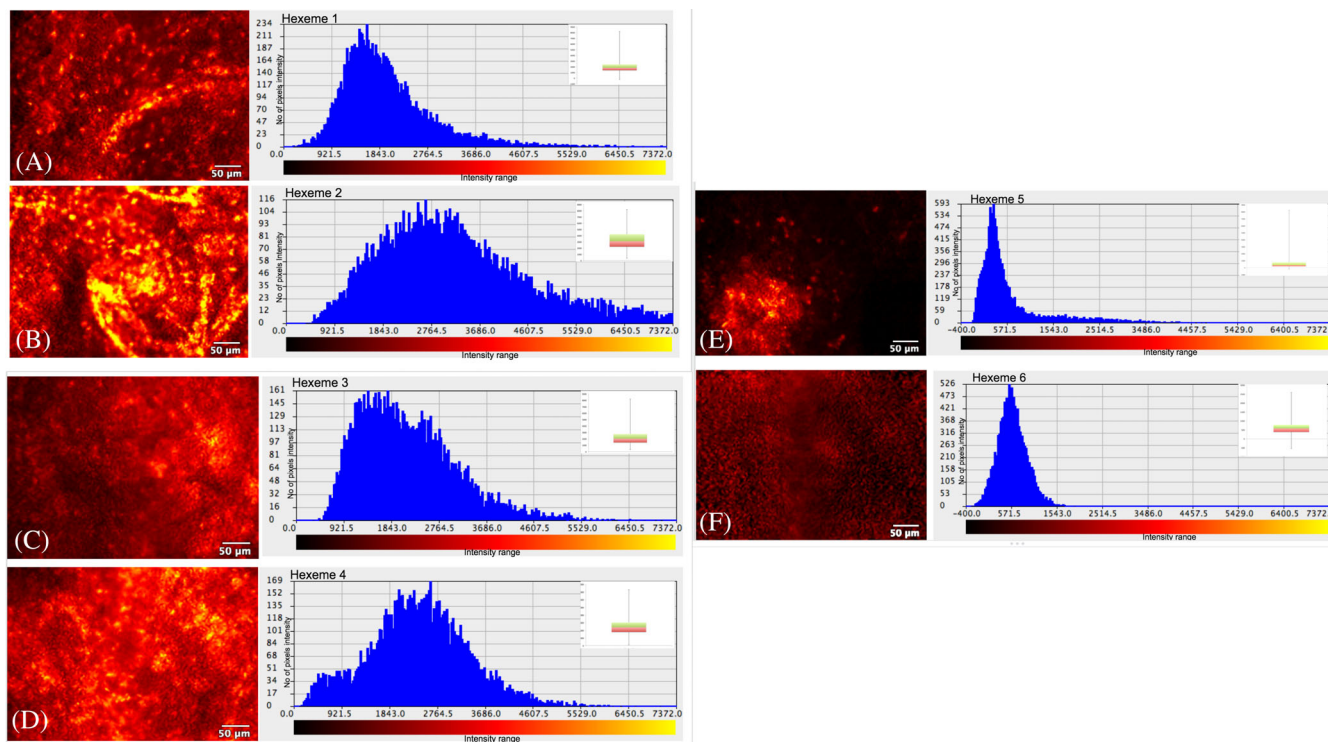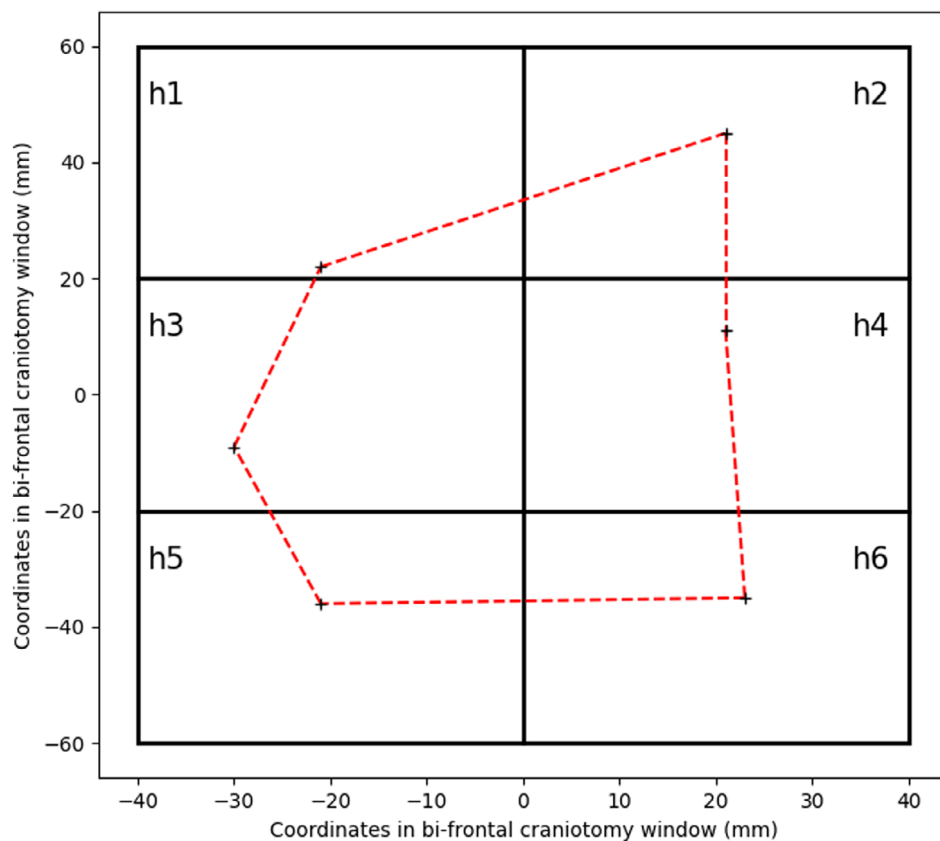
FIGURE 11 Illustrates the p-CLE images captured for each hexeme with its image histograms separated into 256 bins with a *Y*-axis of intensity pixels, illustrating various captured images of the tissue. (A) Hexeme 1 with a median intensity 1813 (LQ = 1398, UQ = 2398, IQR = 1000), (B) hexeme 2 with a median intensity value of 3091 (LQ = 2219, UQ = 4206, IQR = 1987), (C) hexeme 3 with a median intensity value 2016 (LQ = 1431, UQ = 2734, IQR = 1303), (D) hexeme 4 with a median intensity value of 2397 (LQ = 1789, UQ = 3023, IQR = 1234), (E) hexeme 5 with a median intensity value of 367 (LQ = 206, UQ = 771, IQR = 565) and (F) hexeme 6 with a median intensity value of 572 (LQ = 383, UQ = 780, IQR 397). Significant difference was observed between hexemes *P* = .000. Prominent vitiligo distribution of high spots suggestive of nuclei are also shown. p-CLE, probe-based confocal laser endomicroscopy

optical biopsies, as well as in developing robust motion control schemes.

5 | CONCLUSION

Practical robotic platforms have huge economic expenditures associated with manufacturing, commissioning and maintenance. This limits their adoption in state run hospitals in the UK and most parts of the developing world may not even have access to it for precision surgery. As part of the design of robotic systems, end-effectors require significant research investment to support continuous innovation. The materials used in developing the soft robot were inexpensive, and custom fabrication enables rapid and convenient iterative design of new systems tailored to certain specifications or functionalities. Soft robotic end-effector systems are practical for neurosurgical applications as they offer significant advantages over rigid body systems and are potentially much safer by reducing the amount of pressure placed on the brain tissue. Various materials including silicone rubbers and novel hydrogels can offer the ability to design these end-effector systems in a cost effective way. We demonstrate that they can be used to support probe-based endomicroscopic image acquisition with minimal image distortion and can capture a wider range of optical biopsy image distributions.

DATA AVAILABILITY STATEMENT

The data that support the findings of this study are available on request from the corresponding author. The data are not publicly available due to privacy or ethical restrictions.

ORCID

Joseph D. Davids https://orcid.org/0000-0002-9257-6722
Joao Cartucho https://orcid.org/0000-0001-8600-2979
Alex James Thompson https://orcid.org/0000-0002-2485-1550
Saina Akhond https://orcid.org/0000-0003-1314-1921
Mark Runciman https://orcid.org/0000-0003-0782-5729
George Mylonas https://orcid.org/0000-0003-3725-5843
Stamatia Giannarou https://orcid.org/0000-0002-8745-1343
James Avery https://orcid.org/0000-0002-4015-1802

REFERENCES

[1] E. Abbey, F. Yang, L. Qi, J. J. Wu, L. Tong, Z. Zhen, *Int. J. Surg. Case Rep.* **2021**, *81*, 105818.

[2] M. Abdel Khalek, V. Joshi, E. Kandil, *Minimally Invasive Therapy Allied Technol.* **2011**, *20*, 360.

[3] V. A. Abdullatif, J. Davis, C. Cavayero, A. Toenniessen, R. J. Nelson, *Urology* **2022**, *161*, 153.

[4] A. Agnino, A. Graniero, N. Villari, C. Roscitano, P. Gerometta, G. Albano, A. Anselmi, *J. Cardiovasc. Med. (Hagerstown)* **2022**, *23*, 399.

[5] A. Ahmad, J. D. Carleton, Z. F. Ahmad, A. Agarwala, *Surg. Endosc.* **2016**, *30*, 3792.

[6] N. Z. Ahmad, S. Naqvi, F. Sagias, H. Stein, M. Harper, J. S. Khan, *Tech. Coloproctol.* **2018**, *22*, 449.

[7] S. AlMasri, A. Y. Hammad, A. H. Zureikat, *J. Gastrointest. Surg.* **2022**, *26*, 989.

[8] O. B. Argun, P. Mourmouris, I. Tufek, C. Obek, M. B. Tuna, S. Keskin, A. R. Kural, *J. Soc. Laparoendosc. Surg.* **2016**, *20*, e2016.00019.

[9] F. R. Arkoncel, J. W. Lee, K. H. Rha, W. K. Han, H. B. Jeoung, C. K. Oh, *Urology* **2011**, *78*, 581.

[10] P. R. Armijo, B. Pokala, L. Flores, S. Hosein, D. Oleynikov, *Updat. Surg.* **2020**, *72*, 179.

[11] H. Arshad, K. Durmus, E. Ozer, *Eur. Arch. Otorhinolaryngol.* **2013**, *270*, 1737.

[12] H. Aselmann, J. H. Egberts, J. H. Beckmann, H. Stein, C. Schafmayer, S. Hinz, B. Reichert, T. Becker, *Chirurg* **2017**, *88*, 411.

[13] H. Aselmann, T. Möller, J. N. Kersebaum, J. H. Egberts, R. Croner, M. Brunner, R. Grützmann, T. Becker, *Chirurg* **2017**, *88*, 476.

[14] A. Ayav, L. Bresler, J. Hubert, L. Brunaud, P. Boissel, *Surg. Endosc.* **2005**, *19*, 1200.

[15] S. Azadi, I. C. Green, A. Arnold, M. Truong, J. Potts, M. A. Martino, *J. Minim. Invasive Gynecol.* **2021**, *28*, 490.

[16] A. Tan, H. Ashrafian, A. J. Scott, S. E. Mason, L. Harling, T. Athanasiou, A. Darzi, *Surg. Endosc.* **2016**, *30*, 4330.

[17] R. Andrews, R. Mah, A. Galvagni, M. Guerrero, R. Papasin, M. Wallace, J. Winters, *Stereotact. Funct. Neurosurg.* **1997**, *68*, 72.

[18] W. Dawes, H. J. Marcus, M. Tisdall, K. Aquilina, *J. Robot. Surg.* **2019**, *13*, 575.

[19] Y. Gong, D. Hu, B. Hannaford, E. J. Seibel, *Proc. SPIE Int. Soc. Opt. Eng.* **2015**, *9415*, 94150C.

[20] Y. Gong, T. D. Soper, V. W. Hou, D. Hu, B. Hannaford, E. J. Seibel, *Proc. SPIE Int. Soc. Opt. Eng.* **2014**, *9036*, 90362S.

[21] D. Hu, Y. Gong, E. Seibel, L. Sekhar, B. Hannaford, *Int. J. Med. Robot. Comput. Assist. Surg.* **2018**, *14*(1), e1872. https://doi.org/10.1002/rcs.1872

[22] A. De Barros, J. F. Zaldivar-Jolissaint, D. Hoffmann, A.-S. Job-Chapron, L. Minotti, P. Kahane, E. De Schlichting, S. Chabardès, *Front. Neurol.* **2020**, *11*, 1033.

[23] P. C. Ashok, M. E. Giardini, K. Dholakia, W. Sibbett, *J. Biophotonics* **2014**, *7*(1–2), 103.

[24] H. Liao, M. Noguchi, T. Maruyama, Y. Muragaki, E. Kobayashi, H. Iseki, I. Sakuma, *Med. Image Anal.* **2012**, *16*, 754.

[25] M. Aubreville, M. Goncalves, C. Knipfer, N. Oetter, T. Würfl, H. Neumann, F. Stelzle, C. Bohr, A. Maier, in *11th Int. Joint Conf. Biomedical Engineering Systems and Technologies, BIOSTEC 2018* (Eds: S. Bermudez i Badia, A. Cliquet, S. Wiebe, R. Zwiggelaar, P. Anderson, A. Fred, H. Gamboa, G. Saggio), Springer Verlag **2019**, Vol. 1024, pp. 67–85.

[26] M. Aubreville, M. Stoeve, N. Oetter, M. Goncalves, C. Knipfer, H. Neumann, C. Bohr, F. Stelzle, A. Maier, *Int. J. Comput. Assist. Radiol. Surg.* **2019**, *14*, 31.

[27] D. Breuskin, J. Szczygielski, S. Urbschat, Y. J. Kim, J. Oertel, *World Neurosurg.* **2017**, *100*, 180.

[28] P. Charalampaki, P. Md, M. Javed, S. Daali, H.-J. Heiroth, A. Igressa, F. Weber, P. Md, *Neurosurgery* **2015**, *62*, 171.

[29] M. Izadyyazdanabadi, E. Belykh, C. Cavallo, X. Zhao, S. Gandhi, L. B. Moreira, J. Eschbacher, P. Nakaji, M. C. Preul, Y. Yang, in *21st Int. Conf. Medical Image Computing and Computer Assisted Intervention, MICCAI 2018* (Eds: G. Fichtinger, C. Davatzikos, C. Alberola-Lopez, A. F. Frangi, J. A. Schnabel), Springer Verlag **2018**, Vol. 11071 LNCS, pp. 300–308.

[30] M. Izadyyazdanabadi, E. Belykh, M. A. Mooney, J. M. Eschbacher, P. Nakaji, Y. Yang, M. C. Preul, *Front. Oncol.* **2018**, *8*, 240.

[31] M. Lucas, E. I. M. L. Liem, C. D. Savci-Heijink, J. E. Freund, H. A. Marquering, T. G. Van Leeuwen, D. M. De Bruin, *J. Endourol.* **2019**, *33*(11), 930.

[32] J. Wu, Y. C. Wang, B. Dai, D. W. Ye, Y. P. Zhu, *Int. Urol. Nephrol.* **2019**, *51*, 1473.

[33] N. Sanai, J. Eschbacher, G. Hattendorf, S. W. Coons, M. C. Preul, K. A. Smith, P. Nakaji, R. F. Spetzler, *Neurosurgery* **2011**, *68*(Suppl. 2), 282.

[34] C. Xiang, J. Guo, J. Rossiter, *Smart Mater. Struct.* **2019**, *28*, 55034.

[35] C. Lee, Y. H. Park, C. Yoon, S. Noh, C. Lee, Y. Kim, H. C. Kim, H. H. Kim, S. Kim, *Med. Biol. Eng. Comput.* **2015**, *53*, 253.

[36] A. Diodato, M. Brancadoro, G. De Rossi, H. Abidi, D. Dall'Alba, R. Muradore, G. Ciuti, P. Fiorini, A. Menciassi, M. Cianchetti, *Surg. Innov.* **2018**, *25*, 69.

[37] S. Kim, C. Laschi, B. Trimmer, *Trends Biotechnol.* **2013**, *31*, 287.

[38] D. Rus, M. Tolley, *Nature* **2015**, *521*, 467.

[39] Smooth-On, *EcoflexTM Series: Super-Soft, Addition Cure Silicone Rubbers*, Smooth-On, Inc., Macungie, PA **2022**.

[40] J. Avery, M. Runciman, A. Darzi, G. P. Mylonas, in *2019 Int. Conf. Robotics and Automation (ICRA)*, **2019**, pp. 9066–9072, https://doi.org/10.1109/ICRA.2019.8793862.

[41] C. DeLorey, M. Runciman, S. Akhond, J. Avery, G. Mylonas, in *Sensing Soft Robot Actuation with Electrical Impedance Tomography (Poster). 2021 Hamlyn Symposium on Medical Robotics*, **2021**.

[42] J. Desai, R. Patel, A. Ferreira, S. Agrawal, *Encyclopaedia of Medical Robotics*, Singapore World Scientific Publishing Co. Pte Ltd, Singapore **2019**. https://www.worldscientific.com/action/showCitFormats?doi=10.1142%2F10770

[43] J. Palep, *J. Minimal Access Surg.* **2009**, *5*(1), 1.

[44] M. Runciman, A. Darzi, G. P. Mylonas, *Soft Robot.* **2019**, *6*, 423.

[45] H. Wang, R. Zhang, W. Chen, X. Wang, R. Pfeifer, *Surg. Endosc.* **2017**, *31*, 3152.

[46] Y. Kim, S. S. Cheng, M. Diakite, R. P. Gullapalli, J. M. Simard, J. P. Desai, *IEEE Trans. Robot.* **2017**, *33*, 1386.

[47] M. W. Gifari, H. Naghibi, S. Stramigioli, M. Abayazid, *Int. J. Med. Robot. Comput. Assist. Surg.* **2019**, *15*, e2010.